Biochimica et Biophysica Acta 1838 (2014) 1760–1768

Contents lists available at ScienceDirect

Biochimica et Biophysica Acta

journal homepage: www.elsevier.com/locate/bbamem

# Conformational changes of the histidine ATP-binding cassette transporter studied by double electron–electron resonance spectroscopy

Michael Sippach [a,1], Daniela Weidlich [b,1], Daniel Klose [a], Christoph Abé [a], Johann Klare [a], Erwin Schneider [b], Heinz-Jürgen Steinhoff [a,*]

[a] Fachbereich Physik, Universität Osnabrück, Barbarastr.7, 49076 Osnabrück, Germany
[b] Institut für Biologie, AG Bakterienphysiologie, Humboldt Universität zu Berlin, Chausseestr. 117, D-10115 Berlin, Germany

ARTICLE INFO

*Article history:*
Received 16 September 2013
Received in revised form 6 February 2014
Accepted 18 February 2014
Available online 26 February 2014

*Keywords:*
ABC transporter
Histidine transporter
Site-directed spin labeling
EPR
Double electron–electron resonance

ABSTRACT

The conformational dynamics of the histidine ABC transporter $HisQMP_2$ from *Salmonella enterica* serovar Typhimurium, reconstituted into liposomes, is studied by site-directed spin labeling and double electron–electron resonance spectroscopy in the absence of nucleotides, in the ATP-bound, and in the post-hydrolysis state. The results show that the inter-dimer distances as measured between the Q-loops of $HisP_2$ in the intact transporter resemble those determined for the maltose transporter in all three states of the hydrolysis cycle. Only in the presence of liganded HisJ the closed conformation of the nucleotide binding sites is achieved revealing the transmembrane communication of the presence of substrate. Two conformational states can be distinguished for the periplasmic moiety of $HisQMP_2$ as detected by differences in distributions of interspin distances between positions 86 and 96 or 104 and 197. The observed conformational changes are correlated to proposed open, semi-open and closed conformations of the nucleotide binding domains $HisP_2$. Our results are in line with a rearrangement of transmembrane helices 4 and 4′ of HisQM during the closed to the semi-open transition of $HisP_2$ driven by the reorientation of the coupled helices 3a and 3b to occur upon hydrolysis.



## 1. Introduction

ATP-binding cassette (ABC) transporters are cellular devices for the ATP-driven translocation of solutes across biological membranes. They operate in organisms from bacteria to man and are involved in a large variety of physiological processes [1]. In mammalian cells, ABC transporters for example play an important role in the immune system or, when mutated, often cause inheritable diseases, such as cystic fibrosis. In plants, more than hundred ABC transporters have been identified in the genomes of *Arabidopsis* and rice. In prokaryotes, ABC transporters mediate the uptake of numerous nutrients and vitamins or the export of toxic compounds or virulence factors in case of pathogens [2]. ABC transporters minimally consist of four protein modules: two transmembrane domains (TMD) forming the translocation path and two nucleotide-binding and -hydrolyzing domains (NBD) [3]. In canonical ABC importers that are confined to prokaryotes, an extracytoplasmic substrate binding protein (SBP) is required as an additional component [4].

SBPs generally consist of two symmetrical lobes or domains, which both display an α-/β-fold, connected by a hinge region [5]. Substrate binding causes a rotation of these lobes towards each other, rendering the central cleft inaccessible from the aqueous surrounding ('Venus-flytrap'-model). Based on more than 120 three-dimensional structures, a classification of SBPs into six clusters was recently proposed [5].

SBPs bind their substrates with high specificity and high affinities, displaying dissociation constants typically ranging from 0.01 to 10 μM [5]. Since prokaryotes usually thrive in a nutrient-limited environment, the capture and accumulation of substrate in proximity to the transporter are considered as main functions of SBPs. However, as these proteins are also indispensable at very high substrate concentrations, they play an important functional role in the catalytic cycle of the transporter [6,7].

Based on structural and biochemical studies, canonical ABC importers may be subdivided into types I and II [8]. The first type comprises importers featuring a transmembrane core of 10–14 helices, like the maltose and histidine transporters. Type II importers on the other hand display larger transmembrane domains with up to 20 helices and specificity for metal chelates, heme, or vitamin $B_{12}$. Moreover, there is growing experimental evidence that the mode of action of both types of transporters may be different [9–12].

The wealth of available biochemical, biophysical and structural data have made the maltose transporter of *Escherichia coli* ($MalE–FGK_2$) a paradigm for type I importers [13,14]. These and other data [15] have

*Abbreviations:* ABC, ATP-binding-cassette; EPR, electron paramagnetic resonance; cw, continuous wave; DEER, double electron–electron resonance; MTSSL, methanethiosulfonate spin label; NBD, nucleotide-binding domain; TMD, transmembrane domain

* Corresponding author. Tel.: +49 541 9692675; fax: +49 541 9692656.
*E-mail address:* hsteinho@uos.de (H.-J. Steinhoff).

[1] M. Sippach and D. Weidlich contributed equally to this work.

http://dx.doi.org/10.1016/j.bbamem.2014.02.010
0005-2736/

substantially supported the 'alternate access' model for type I ABC importers. Accordingly, in the absence of substrate, the transporter resides in the inward-facing (resting) state and might be in contact to the cognate SBP [16,17]. Furthermore, due to the high (mM) concentration of ATP in the bacterial cytoplasm, the resting state of the transporter is assumed to have ATP bound to the NBDs which, where analyzed, exhibit dissociation constants for ATP in the μM range [18]. Upon binding of substrate, SBP is shifted to its closed conformation, which in turn promotes a tight association of the NBDs [6,17], resulting in the opening of the transport path to the extracellular side ('outward-facing'). Concomitantly, SBP is pushed towards its open conformation and the substrate is released to a putative binding site within the transmembrane core, for which structural evidence is available for the maltose transporter [19]. At this stage, SBP forms a stable complex with the transporter. Subsequently, hydrolysis of both ATP molecules which might occur sequentially, allows the release of the substrate to the cytoplasm. Eventually, the dissociation of phosphate and ADP, and rebinding of ATP would restore the resting state.

However, there are distinctive features by which the maltose transporter differs from the vast majority of other type I ABC importers: (i) large periplasmic loops of its TMDs, in particular, loop P2 of the MalF subunit encompassing 183 amino acid residues, that are crucial for binding protein–transporter interaction and transmembrane signaling [16,19–23], are absent in most ABC importers; and (ii) the C-terminal extension of MalK which structurally supports the observed tweezers-like conformational change of the MalK dimer upon ATP binding [24] is largely confined to MalK homologs of the CUT1 subfamily [25]. Thus, the question arises whether a transport model based on the maltose system is generally applicable to other type I ABC importers. In order to address this question, we have studied the histidine ABC transporter from *Salmonella enterica* serovar Typhimurium (*S.* Typhimurium) which lacks the distinctive features of the maltose transporter described above. Although structural information on the full transporter is elusive, the histidine transporter, next to the maltose transporter, is still the best-studied type I importer to date [26,27]. It is composed of the transmembrane subunits, HisQ and HisM, and a homodimer of the nucleotide-binding subunit, HisP, of which a (monomeric) crystal structure is available [28]. Two SBPs, with the highest affinities for histidine (HisJ) and lysine, arginine, and ornithine (LAO), respectively, have also been characterized in great detail [29,30].

Here, we report on the dynamics of the histidine transporter, incorporated into liposomes, in the absence of nucleotides, in the ATP-bound, and in the post-hydrolysis state as studied by continuous wave (cw) and double electron–electron resonance (DEER) spectroscopy. Our results show that the inter-dimer distances measured between the Q-loops of $HisP_2$ resemble those determined for MalK in all three states of the hydrolysis cycle investigated. We show that in the presence of ATP only upon addition of liganded HisJ the closed conformation of the NBDs is achieved. The resolved rearrangements of the TMDs initiated by ATP hydrolysis are in line with respective conformational changes observed in $MalFGK_2$.

## 2. Materials and methods

### 2.1. Site-directed mutagenesis

Plasmids used in this study are listed in Table 1. Cysteine residues were introduced by Stratagene QuikChange Lightning kit using plasmids pDW42 (cysless) or pDW75 (HisM-C114) as templates.

### 2.2. Purification of $HisQMP_2$ complexes

Cells of *E. coli* BL21-T1® (DE3) pLysS were transformed with the respective plasmids and grown in TB(Amp/Cam)-medium at 30 °C and 180 rpm shaking till an $OD_{650\ nm}$ of 0.8–1 was reached. Overexpression of transporter genes was induced with 0.1 mM IPTG, the temperature reduced to 22 °C and growth continued for 4 h. Cells were harvested, resuspended in 50 mM Tris/HCl (pH 7.5), 10% glycerol, 0.1 mM phenylmethylsulfonyl fluoride (PMSF) and disintegrated by passage through a high pressure cell disrupter (1.3 kbar) (Model Basic Z, Constant Systems Ltd., Northamptonshire, England). After low speed centrifugation (10,000 *g*, 10 min, 4 °C), the membrane fraction was collected by ultracentrifugation for 90 min (200,000 *g*) and subsequently solubilised with 1.1% n-dodecyl-β-maltoside (DDM) at a protein concentration of 10 mg/ml for 1 h at 4 °C. After ultracentrifugation, the supernatant was subjected to metal-affinity chromatography using TALON resin (Clontech) previously equilibrated in 50 mM Tris/HCL (pH 7.5), 20% glycerol, 0.05% DDM, 100 mM NaCl, 4 mM β-mercaptoethanol and 0.1 mM PMSF. After several washing steps, complex protein was eluted with the same buffer supplemented with 100 mM imidazole. Protein containing fractions were pooled, concentrated with a centrifugal devise, passed through a PD-10 column, equilibrated with 50 mM MOPS/KOH (pH 7.5), 20% glycerol, 0.05% DDM, and 100 mM NaCl, and subsequently stored at −80 °C.

**Table 1**
Plasmids used in this study.

| Plasmid | Relevant genotype or description | Reference or source |
|---|---|---|
| *hisJ* | | |
| pET15b | $Ap^r$, $p_{T7lac}$, $His_6$ coding sequence (5′), thrombin cleavage site (expression vector for *hisJ*) | Novagen |
| pSN2 | *hisJ* | Lab collection |
| *hisQMP* | | |
| pET22b | $Ap^r$, $p_{T7lac}$, $His_6$ coding sequence (3′) (expression vector for *hisQMP* alleles) | Novagen |
| pVE26 | *hisQMP* | [53] |
| pDW42 | *hisQ*(C197S)*M*(C104S,C114S,C149S)*P*(C51S) | This study |
| pDW38 | *hisQM*(C114S,C149S)*P*(C51S) | This study |
| pDW43 | *hisQ*(C197S)*M*(C104S,C114S,C149S)*P*(C51S,H101C) | This study |
| pDW69 | *hisQ*(C197S)M(C104S, C114S, C149S)*P*(C51S,H153C) | This study |
| pDW75 | *hisQ*(T109C,C197S)*M*(C104S,C149S)*P*(C51S) | This study |
| pDW103 | *hisQ*(A118C,C197S)*M*(C104S,C114S,G123C,C149S) *P*(C51S) | This study |
| pDW114 | *hisQ*(D86C,C197S)*M*(A96C,C104S,C114S,C149S) *P*(C51S) | This study |

### 2.3. Spin-labeling of $HisQMP_2$ complexes and reconstitution

Purified complex protein was incubated with 10 fold molar excess (1-oxyl-2,2,5,5-tetramethylpyrroline-3-methyl) methanethiosulfonate (MTSSL) for 4 h at 4 °C or overnight under gentle stirring in the dark. Unbound label was subsequently removed by passage through a PD-10-column and protein was concentrated using Amicon® Ultra-4 Centrifugal Filter Units, YM10 (Millipore, Bedford, USA) up to 3 mg/ml. Reconstitution into *E. coli* total Lipid Extract (Avanti Polar Lipids, Inc., Alabaster, USA) was performed at a 5:1 lipid to protein ratio in a final volume of 1 ml. Detergent was removed using BioBeads (Bio-Beads SM-2 Adsorbent, BioRad) overnight. After replacing the beads with a new batch, incubation continued for 2 h. Proteoliposomes were collected by ultracentrifugation and resuspended in 50 mM MOPS/KOH (pH 7.5) to reach a final complex concentration of 100 μM. To mimic different steps of the transport cycle and if not stated otherwise, samples were supplemented with 100 μM HisJ/1 mM histidine in the presence of 10 mM ATP/1 mM EDTA (added during reconstitution), or 2 mM ATP/3 mM $MgCl_2$. $Mg^{2+}$-ions permeabilize the proteoliposomes, thereby allowing access of ATP to the lumen of the vesicles [31]. Under these conditions (1:1 stoichiometry of $HisQMP_2$ to HisJ), a specific ATPase activity of 0.14 μmol $P_i$ $min^{-1}$ $mg^{-1}$ was determined which assured complete hydrolysis of ATP after 30 min at 37 °C. Samples were flash

frozen in liquid nitrogen after transfer into glass capillaries for EPR measurements.

The spin labeling efficiency determined by continuous-wave EPR- and absorption spectroscopy varied between 75 and 95% with the exception of positions HisP101/HisP101′ and HisQ118/HisM123, where the label efficiency is smaller.

### 2.4. Purification of HisJ

For the purification of HisJ, *E. coli* BL21-T1® (DE3) (pLysS, pSN2) was grown in LB(Amp/Cam)-medium at 30 °C and shaking with 180 rpm. Overproduction was induced at $OD_{650\ nm}$ 0.5 with 0.5 mM IPTG and cell growth continued for 3 h. After cell disruption as described for $HisQMP_2$, the cytosolic fraction was subjected to a TALON resin, equilibrated with 50 mM Tris/HCl (pH 7.5), 10% glycerol, 150 mM NaCl and 0.1 mM PMSF. Following a washing step with 10 mM imidazole, elution of his-tagged HisJ was achieved by washing the matrix with the same buffer supplemented with 250 mM imidazole. After concentrating the protein containing fractions to 2.5 ml, imidazole was removed by gel filtration (PD-10-column) and the protein was flash-frozen in liquid nitrogen and stored at −80 °C.

### 2.5. ATPase assay

Assaying the ATPase activity of reconstituted complex variants before and after spin-labeling was performed according to Nikaido et al. [32] and as described in Weidlich et al. [33].

### 2.6. Continuous wave EPR experiments

EPR spectra for interspin distance determination were recorded at 160 K using a homemade EPR spectrometer equipped with a Bruker high-Q cavity. The magnetic field was measured with a B-NM 12 B-field meter (Bruker, Rheinstetten, Germany). A continuous flow cryostat Oxford ESR 900 allowed stabilization of the sample temperature to 160 K. The microwave power was set to 0.2 mW and the B-field modulation amplitude adjusted to 0.25 mT. Samples were loaded into EPR quartz capillaries (3 mm inner diameter, sample volume 40 μl).

### 2.7. Fitting of simulated continuous wave low temperature EPR spectra

Fitting of simulated dipolar broadened EPR powder spectra to the experimental ones recorded at 160 K was carried out according to the method described by Steinhoff et al. [34]. Owing to the flexible spin-label side chain, a random distribution of nitroxide ring orientation with respect to the interspin distance vector is assumed. To account for a range of distances expected to arise from these different orientations, a Gaussian distribution of interspin distances is allowed. During the fitting procedure, the g-tensor values, two components of the A-tensor ($A_{xx}$ and $A_{yy}$), and the line width parameters were fixed according to the values found from analysis samples where dipolar broadening is absent. The parameters used are $g_{xx} = 2.0082$, $g_{yy} = 2.0062$, $g_{zz} = 2.0023$, $A_{xx} = 0.52$ mT, and $A_{yy} = 0.45$ mT, and $A_{zz}$ was the variable to account for different polarities of the SL environment. The distance distribution width was fixed to 0.5 nm. To fit the dipolar broadened spectrum for the respective mutant in different states, the average interspin distance and $A_{zz}$ were allowed to vary.

### 2.8. Pulse EPR experiments

DEER experiments were performed at X-band frequencies (9.3–9.4 GHz) with a Bruker Elexsys 580 spectrometer equipped with a Bruker Flexline split-ring resonator ER 4118X-MS3 and a continuous flow helium cryostat (CF935; Oxford Instruments) controlled by an Oxford Intelligent Temperature Controller ITC 503S. All measurements were performed using the four-pulse DEER sequence: $\pi/2(\upsilon_{obs}) - \tau_1 - \pi(\upsilon_{obs}) - t' - \pi(\upsilon_{pump}) - (\tau_1 + \tau_2 - t') - \pi(\upsilon_{obs}) - \tau_2 -$ echo [35]. A two-step phase cycling (+ ‹x›, − ‹x›) was performed on $\pi/2(\upsilon_{obs})$. Time $t'$ is varied, whereas $\tau_1$ and $\tau_2$ are kept constant. The dipolar evolution time is given by $t = t' - \tau_1$. Data were analyzed only for $t > 0$. The resonator was overcoupled and the pump frequency $\upsilon_{pump}$ was set to the center of the resonator dip (coinciding with the maximum of the nitroxide EPR spectrum) whereas the observer frequency $\upsilon_{obs}$ was 65 MHz higher (low field local maximum of the spectrum). All measurements were performed at a temperature of 50 K with observer pulse lengths of 16 ns for π/2 and 32 ns for π pulses and a pump pulse length of 12 ns. Proton modulation was averaged by adding traces at eight different $\tau_1$ values, starting at $\tau_{1,0} = 200$ ns and incrementing by $\Delta\tau_1 = 8$ ns. Data points were collected in 8 ns time steps or, if the absence of fractions in the distance distribution below an appropriate threshold was checked experimentally, in 16 ns time steps. The total measurement time for each sample was 24 h. Analysis of the data was performed with DeerAnalysis2011 [36].

### 2.9. Spin label side chain rotamers and normal mode analysis

#### 2.9.1. Static rotamer library analysis

The rotamer analysis provides the conformational distribution of the spin label side chain R1 at any chosen position in the otherwise fixed protein structure using a library of precalculated rotamers as described in detail in [37]. In brief, the superposition of the R1's backbone atoms onto the protein backbone at the respective position provides the orientations of R1 with respect to the protein structure and allows for the calculation of a resulting energy for the R1–protein interaction from the Lennard Jones potential. Subsequent Boltzmann weighting and normalization by the partition function yields a probability for each rotamer which is then multiplied by the probability of R1 to exhibit each conformation. This results in the final rotamer probability distribution at the site of interest. Between two such probability distributions at two positions in the protein, a distance distribution is calculated as the histogram of all pairwise inter-spin distances weighted by the product of their respective probabilities. The RLA is performed with the freely available software package MMM (Multiscale Modeling of Macromolecules, version 2010) with $HisQMP_2$ homology model used as input and MTSSL at 175 K as rotamer library [37].

#### 2.9.2. Flexible rotamer library analysis

Normal modes of the $HisQMP_2$ ground state given by the homology model were calculated using an anisotropic network model with a Cα interaction cutoff of 10 Å and a distance weight of 2.5 as implemented in the ANM webserver [38]. Resulting normal modes were obtained as PDB files with 20 frames and an amplitude scale of 35. The static RLA results were combined with the normal modes in a rigid domain approximation in VMD [39] where each of the four domains (HisQ, HisM, HisP, HisP′) of the spin labeled homology model was fit to the respective normal mode coordinates and a distance distribution was calculated at each step using the ground state rotamer weights from the static RLA. VMD with Stride [40] secondary structure assignment and NMWiz was used for visualization and Tachyon for rendering [41].

## 3. Results

### 3.1. The experimental system

Fig. 1 shows the spin labeled sites in the structure of the histidine ABC importer which was modeled according to the coordinates of the *E. coli* methionine transporter MetNI (PDB ID: 3DHW) [33]. As in the case of HisQ and HisM, but unlike all other ABC transporter with solved X-ray structure, the transmembrane subunit MetI of the methionine transporter spans the membrane only five times. To simultaneously detect conformational changes of the nucleotide-binding domains and

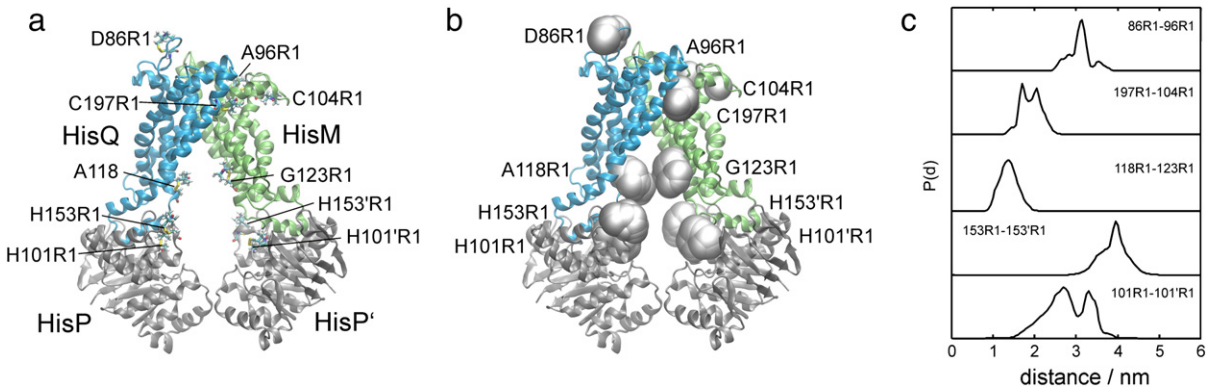


**Fig. 1.** Model of $HisQMP_2$ based on the structure of the methionine transporter MetNI (PDB ID: 3DHW). a) A single rotamer of each of the spin label side chains (denoted R1) is depicted in stick representation at the indicated sites. b) The nitroxide group spatial distributions are highlighted by gray surfaces. c) Distance distributions, P(d), between different spin labels calculated from the rotamer ensembles shown in b).

transmembrane domain rearrangements accompanying the ATP hydrolysis cycle spin labels were introduced at different sites in the TMDs and in the NBDs as highlighted in Fig. 1a. The figure depicts a single possible rotamer of each of the bound spin label side chains. The distance vector between positions D86 in HisQ and A96 in HisM spans the putative periplasmic gate, whereas the native cysteines C104 (HisM) and C197 (HisQ) are located closer to its periphery. Sites A118 (HisQ) and G123 (HisM) are located at the cytoplasmic ends of helices 3 (HisQ) and 3′ (HisM). The vector connecting these sites spans the cytoplasmic gate. The NBD positions 101/101′ were chosen to determine conformational transitions of the NBDs, as the homologous site of MalK, position 83, has been proven to be suited for this purpose [42].

Cysteines were introduced pairwise and modified with MTSSL and assayed for ATPase activity in proteoliposomes. Compared to wild type $HisQMP_2$ ($0.68 \pm 0.05$ μmol $P_i$ $min^{-1}$ $mg^{-1}$) the cysless variant used as a control, displayed a specific ATPase activity of $0.44 \pm 0.04$ μmol Pi $min^{-1}$ $mg^{-1}$ in the presence HisJ/histidine. Thus, the replacement of all four native cysteine residues by serines caused some reduction in enzymatic activity. However, for both wild type and cysless variants about threefold stimulation was observed compared with the intrinsic activity, suggesting functional coupling of ATP hydrolysis to substrate transport. Moreover, at the amount of HisJ used here (1 μmol), the observed activities are consistent with those reported in a previous study [26]. Stimulation of the double cysteine complexes ranged from 2-fold to 3.4-fold before spin-labeling and from 1.6-fold to 2.4-fold after modification with MTSSL, except for HisQ(C197R1)HisM(C194R1)$P_2$ (hereafter R1 will denote the unnatural side chain carrying the nitroxide radical), which could no longer be stimulated, most probably due to an interference of the modifications with HisJ interaction. Thus, the latter is considered representative of the intrinsic (uncoupled) ATPase activity of the transporter.

### 3.2. Interspin distance simulation based on a rotamer library approach

In order to visualize the spin labeled complex shown in Fig. 1a and to enable comparison between the EPR data and the structural model, in silico spin-labeling of the above positions was carried out. The simulation of the expected interspin distances was obtained based on a rotamer library approach implemented in the software MMM [43]. The simulation provides the spin label rotamers which can be populated in the structure and predicts the distances between the nitroxides of two labeled sites. The results of the simulations are presented in Fig. 1b and c. Fig. 1b shows the spaces covered by each rotamer ensemble, Fig. 1c displays the corresponding calculated interspin distances under the assumption that the above model for the nucleotide free $HisQMP_2$ is valid. The distance distribution for the pair 101R1–101′R1 exhibits maxima between 2.5 and 3.5 nm, the distance distribution for the pair 153R1–153′R1 is centered between 3.5 and 4.5 nm. The chosen sites in the transmembrane domains cover the distance range from 1.5 nm (118R1–123R1) to 3.2 nm (86R1–96R1). This distance range is accessible for DEER spectroscopy (also known as pulse electron double resonance, PELDOR), which has been used to determine inter-residual distances in spin labeled soluble and membrane proteins as well as in nucleic acids (for a review cf. [44]). For distances below 2 nm low temperature ($T = 160$ K) cw EPR spectroscopy complements the DEER data.

### 3.3. Interspin distances reveal conformational changes upon ATP binding and hydrolysis

In the following DEER spectroscopy is applied to determine the interspin distances between the pairs of spin label R1 side chains shown in Fig. 1a. The purified $HisQMP_2$ complexes were reconstituted into liposomes and measured in the presence of histidine and HisJ in three different states: in the absence of nucleotides (apo-state), in the presence of ATP and EDTA to prevent hydrolysis, and in the post hydrolytic state. This state was obtained by incubation with ATP and $MgCl_2$. The hydrolysis of ATP and concomitantly induced conformation transitions of the NBDs were found to be complete within several seconds. However, in order to unify the hydrolysis procedure incubation was performed for 30 min at 37 °C for all samples. The vanadate-trapped conformer, which mimics the transition state during ATP hydrolysis, was analyzed for the spin labeled pair 101R1–101′R1. The DEER data and their analyses are presented in Fig. 2.

The raw DEER data (Fig. 2a, *left*) reveal exponential decay due to a homogeneous multi-dimensional distribution of spins in the samples. In addition pairs 197R1–104R1, 118R1–123R1 and 101R1–101′R1 show strongly damped oscillations within the first 500 ns, unambiguously indicating the presence of intracomplex dipolar interactions. On the contrary, such oscillations are not obvious for 86R1–96R1 and 153R1–153′R1. This is a well known problem for membrane reconstituted proteins and renders the analysis challenging. However, fitting of an exponential representing a three dimensional background of interacting spins reasonably well accounts for the background behavior for those samples where oscillations are obvious. We therefore assumed the same dimensionality to be valid also for 86R1–96R1 and 153R1–153′R1. The comparison of the normalized raw data (Fig. S1, Supplementary material) and of the background corrected data shows that oscillations significantly differ in different states for 197R1–104R1 and 101R1–101′R1, less prominent changes can be deduced for the traces of 86R1–96R1 and 118R1–123R1. Fig. 2a (*right*) represents the form factors, F(t), obtained by dividing V(t) by the background, B(t), and renormalizing at zero time. The small modulation

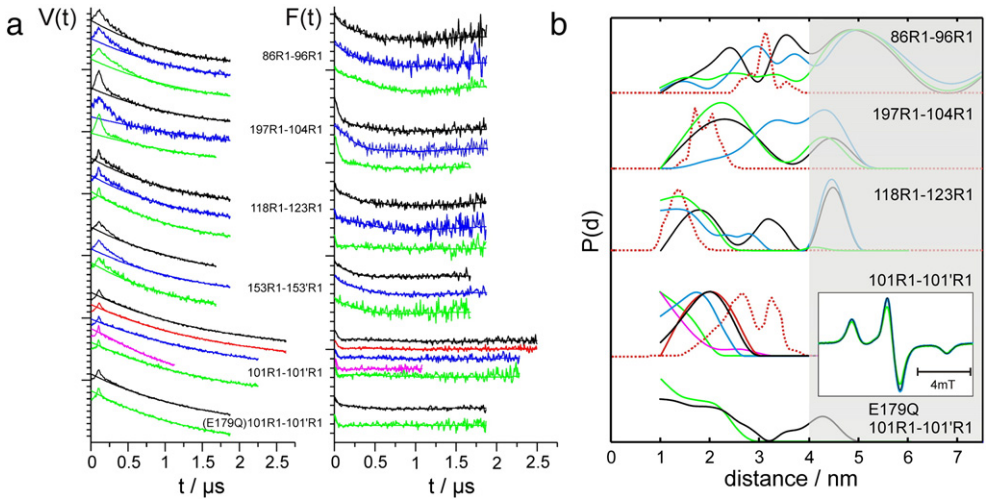


**Fig. 2.** DEER traces and interspin distance distributions for three different states of the nucleotide hydrolysis cycle. a) DEER traces, V(t), and baseline corrected data, F(t), for the apo state (black), the ATP bound state (blue) and the post hydrolysis state (green) in the presence of liganded HisJ. In addition, for positions 101/101′ the data for the vanadate-trapped state (magenta), for the state in the presence of ATP but in the absence of HisJ (red), and for the hydrolysis incompetent mutant E179Q in the absence of any substrate (black) and in the presence of HisJ, ATP and $Mg^{2+}$ (green) are shown. The noiseless lines in the plot of F(t) show the best fit according to the distance distributions depicted in b). Tick separation on the vertical axes is 0.1. b) Distance distributions calculated from the DEER traces shown in a). Tikhonov regularization is applied as implemented in DEERAnalysis2011 [36]. (The data for 153R1–153′R1 are shown in the Supplementary material, Fig. S3.) The gray shaded area above 4 nm indicates limited certainty of the distance data (position and width of the distribution) based on the length of the shortest DEER time trace [36]. In this region inter-complex spin–spin interaction also significantly contributes. The simulated distance distributions shown in Fig. 1c are superimposed (dotted lines) for comparison. The inset shows superimposed continuous wave EPR spectra of 101R1–101′R1 for the apo state (black), the ATP bound state (blue), and the post hydrolysis state (green). The spectra are normalized to the same spin number.

depths of 8–15% obtained for position 101 are due to restricted accessibility of this cysteine towards MTSSL and the presence of interspin distances below 1.6 nm.

Distance distributions, P(d), with maxima at and below 2 nm are found for the pair 101R1–101′R1 for all states investigated (Fig. 2b). This short distance range is borderline between pulse and cw-EPR analysis. cw-EPR spectra (T = 160 K) were recorded on the same samples. The comparison of the cw spectra reveals increased dipolar broadening only upon hydrolysis (inset in Fig. 2b). A line shape analysis by fitting of simulated spectra to the experimental ones of the post hydrolysis state using the program DIPFIT [34], which assumes a Gaussian distance distribution, yields an average distance of 1.4 nm (fittings are depicted in Fig. S2). This result shows the complementary character of the pulse and cw techniques for distances in the 1–2 nm range. According to the results of the DEER data the distance distributions of the apo state and of the ATP-bound state in the absence of HisJ are indistinguishable with their maxima found at 2 nm. Upon addition of liganded HisJ, which accesses half of the reconstituted transporter molecules, the maximum of this distribution shifts to 1.8 nm for the ATP bound state. The validation of the DEER data (Fig. S3) shows that this shift is significant revealing the coupling of HisJ binding to the NBD conformation. The closest approach for the spin label side chains at positions 101 and 101′ is found in the post hydrolysis and in the vanadate-trapped states, which mimics the transition state during ATP hydrolysis.

The distance distribution for 101R1–101R1′ of the hydrolysis incompetent mutant $HisQMP(E179Q)_2$ in the apo state resembles that of the unmutated variant but with a broader distance distribution in the 1 to 3 nm region. In addition, contributions of P(d) fall in the distance range above 3 nm which disappear upon the addition of ATP. This is evidence that complete dimerization of the NBDs in this variant may occur only upon ATP binding. Upon incubation with ATP/$MgCl_2$ the distance distribution displays its major contribution still in the distance range between 1 and 3 nm. In particular, it is not completely shifted below 2 nm as found for the post hydrolysis state of the unmutated variant. E179 has been reported to be the most likely candidate for the catalytic base in the hydrolysis reaction [28]. Our findings are in agreement with the crystal structures of the maltose transporter showing no structural differences between the ATP-bound wild type and the corresponding E159Q mutant [19,45,46].

A detailed comparison of the distance distributions found for 101R1–101R1′ with the changes of simulated distance distributions for the closed, semi-open and open states based on the crystal data of the maltose transporter, $MalFGK_2$, is presented in the discussion section below.

The DEER traces observed for the NBD positions 153–153′ do not reveal clear oscillations. Superposition of the traces, V(t), for the three states does not reveal significant differences (Fig. S1). Tikhonov regularizations yield broad distance distributions with prominent peaks in P(d) between 3 and 5 nm (Fig. S3) which cannot unambiguously be attributed to spin–spin interaction within a NBD dimer. Since population peaks in this distance range are also found in the P(d) plots of 86R1–96R1, 118R1–123R1 and 197R1–104R1 (Fig. 2b) inter-complex interactions are very likely to contribute. Since inter- and intra-molecular interactions cannot be clearly separated no further conclusion is drawn from this experiment.

### *3.4. Conformational changes of $HisP_2$ induce conformational transitions of HisQM*

We examined possible effects of the observed $HisP_2$ conformational rearrangement during the nucleotide hydrolysis cycle on the conformation of the transmembrane domains HisQM under the same experimental conditions. Superposition of the DEER traces of 118R1–123R1 recorded for the three different states reveals different decays (Fig. S1). Distance distributions with two major distance peaks centered at 2 nm and 3.2 nm were found for the apo-state of 118R1–123R1 (Fig. 2b). The contributions above 2.5 nm disappear for the ATP bound and post hydrolysis states and the majority of pair dipole interaction originates from interspin distances less than 1.8 nm. The simulation based on the model yields an average distance of 1.5 nm in agreement with the experimental data of the ATP-bound and post hydrolysis states.

Different DEER traces (Fig. S1) and distinct distance distributions were observed for the pair 197R1–104R1 (Fig. 2b) for the three states investigated. The peak interspin distance of 2.2 nm found in the apo-

state is shifted to 3.2 nm in the ATP-bound state and back to 2.1 nm upon ATP hydrolysis. The defined distributions indicate sterical restricted nitroxide side chains which is in agreement with the powder like room temperature cw-EPR spectrum of this sample (not shown). The experimental interspin distances for the apo and post hydrolysis states resemble the simulated one (1.8–2.1 nm) revealing that the periplasmic moiety of the transmembrane domains is well represented by the model.

The lack of oscillations (Fig. 2a) and the presence of only subtle differences in the DEER traces for the different states of 86R1–96R1 (Fig. S1) render the analysis difficult. With the best background fitting broad distance distributions are found for all three states (Figs. S3 and 2b) most probably reflecting the flexibility of the loop position HisQ-86, and, as in the other cases, inter-complex interaction in the distance range beyond 4 nm. However, in contrast to the data for 153R1–153′R1, here the contributions below 4 nm are well separated from the inter-complex interactions (Figs. 2b, S3). The simulations of interspin distances based on the $HisQMP_2$ model with a fixed backbone yields a distance range between 2.5 and 3.5 nm which is covered by the experimental data. Differences in the DEER data, V(t), for the different states obvious within the first 1 μs (Fig. S1) and corresponding differences in the distance distributions, P(d), (Fig. 2b), reveal conformational changes of the putative periplasmic gate upon ATP hydrolysis.

For all sites but one the correlation between the EPR-derived and the simulated interspin distances based on the HisQM model can be considered as in agreement taking into account the possible backbone flexibility which is not accounted for in the simulations. The only exception is the distance between 101R1 and 101′R1 which is shorter than the modeled one for all states investigated suggesting that the NBDs of $HisQMP_2$ are in closer vicinity than those of MetNI. The behavior of 101R1–101′R1 agrees with that of 83R1–83′R1 of $MalK_2$ as discussed in detail below.

### 3.5. Normal mode analysis and flexible rotamer library approach

In order to analyze which movement of the NBDs is compatible with the changes in the DEER distance distributions, we assess changes of the interspin distances along the first ten modes of the normal mode spectrum of the $HisQMP_2$ model. Such modes are perceived to be relevant for a variety of conformational transitions in membrane proteins [47]. The normal modes, calculated by an anisotropic network model [38,48], are fundamental oscillations around a ground state, which here is given by the modeled $HisQMP_2$ structure containing the spin label rotamers from the static RLA [37]. We follow changes in the interspin distance distributions by calculating distance distributions along each protein oscillation using the ground state spin label rotamers on an oscillating protein backbone.

A normal mode or a linear combination of modes will match the experimental data, if the simulated interspin distance changes of all pairs are correlated to the experimental ones. The first mode representing the lowest oscillation frequency is not related to any significant distance change between the centers of mass of the two NBDs, between positions 118 and 123 or 86 and 96 (Fig. S4 Supplementary material). The second and third modes have in common an equidirectional change of the distances between the centers of mass of the NBDs, for the pairs 101R1–101′R1 and 118R1–123R1, and an opposite behavior for the distance between positions 86 and 96. These two modes thus represent a highly concerted movement of the HisP domains, the cytoplasmic and the periplasmic gate. The forth mode reveals again equidirectional behavior of the distance changes of 101R1–101′R1 and 118R1–123R1. Since this analysis is based on the $HisQMP_2$ model in the apo-state one may conclude that the direction of interspin distance changes of 101–101′R1 and 118–123′R1 is correlated in conformational changes which do not deviate too much from the apo-state conformation.

## 4. Discussion

In order to understand the conformational changes which $HisP_2$ undergoes during the catalytic cycle of the histidine transporter a comparison of our experimental results with those of $MalFGK_2$ is necessary. Crystal structures of isolated *E. coli* $MalK_2$ have been solved in the apo-state, in the ADP- and ATP-bound states, representing the open, a semi-open and a closed conformation of the dimer, respectively [24,49]. For all three states crystal structures of the full transport complex are also available [19,45,46,50]. Based on these structures, the closure and reopening of the MalK dimer have been described as a 'tweezers-like' motion, with the C-terminal domain representing the 'handle' and the N-terminal domains being the 'tips' of the tweezers [24]. The ATP-induced MalK dimer closure was also observed by spin-labeling EPR spectroscopy in detergent micelles and in the presence of substrate-loaded MalE for the complex reconstituted in proteoliposomes [6,16,17,42,51]. ATP hydrolysis was shown to induce a semi-open state of the NBDs in intact transporters that resembles the effects observed in the isolated domains [6]. These three different conformations of $MalK_2$ lead to different distributions of the distances between spin labels bound to the Q-loop positions 83 and 83′ in the dimer as revealed by a rotamer analysis (Fig. 3a). In the open conformation of $MalK_2$ found for the apo-state of the full complex (PDB ID: 3FH6) the distances between the nitroxides cover the range from 1.5 to 2.8 nm with population maxima between 2.2 and 2.6 nm. For the semi-open conformation of $MalK_2$ (PDB ID: 3PV0, 3PUZ) the maximum of the

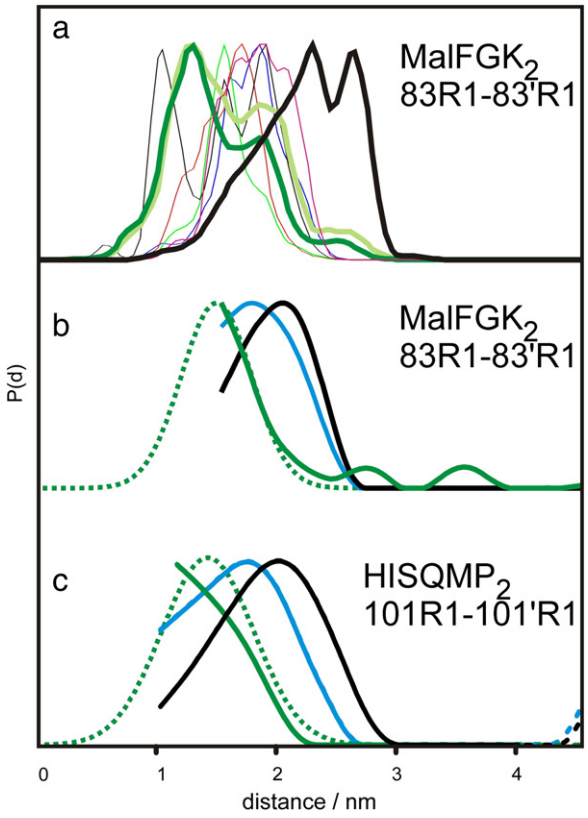


**Fig. 3.** Comparison of the distance distributions determined for the spin label pair 101R1–101′R1 in $HisP_2$ with those for 83R1–83′R1 in $MalK_2$. a) Rotamer analysis of inter-nitroxide distance distributions for 83R1–83′R1 based on crystal data of the open state of $MalK_2$ (thick black line PDB ID: 3FH6), of semi-open states (thick lines, light green PDB ID: 3PUZ; dark green PDB ID: 3PV0), and of closed conformations of $MalK_2$ (thin lines, blue PDB ID: 3PUV; green PDB ID: 3PUW; red PDB ID: 2R6G; black PDB ID: 3RLF; magenta PDB ID: 3PUY). Experimental inter-nitroxide distances determined for the apo-states (black), for the ATP-bound states (blue) and for the post hydrolysis states (green), based on DEER data (continuous lines) and cw-EPR spectroscopy (dashed lines) are shown in b) for 83R1–83′R1 in $MalK_2$ [42] and in c) for 101R1–101′R1 in $HisP_2$ (this work).

distribution is shifted to 1.2 nm. Inter-nitroxide distance distributions calculated for five different crystal structures exhibiting the closed state of $MalK_2$ (PDB ID: 3PUV, 3PUY, 3PUW, 2R6G, 3RLF) agree in the location of their population maxima between 1.5 and 1.9 nm, thus at significantly larger distances compared to the semi-open state. This is unexpected because the Cα atoms of residues 83 and 83′ show their closest approach in the closed conformation. The structural models of $MalK_2$ (Fig. S5) reveal that the rotamers of the spin label side chains are differently populated in the semi-open compared to the closed conformation of $MalK_2$ due to different sterical constraints. The smallest average distance between the nitroxides is thus observed in the semi-open conformation. Small differences in the conformations of the closed state are sensitively reflected in the calculated distance distributions as, e.g., a significant contribution at a distance of 1 nm is found only for the crystal structure 3RLF and not for the other closed conformations of $MalK_2$. Fig. 3b shows that the experimentally determined interspin distance distributions reported in reference [42] are in reasonable agreement with the rotamer calculations with the largest distances found for the apo state and the closest approach found for the post hydrolysis state representing the semi-open state. It is worth noting that a fully opened state of the NBDs as observed for the apo state in the crystallized conformation (3FH6) should exhibit inter nitroxide distances up to 2.6 nm. In contrast the DEER distance distributions reported for $MalFGK_2$ in the absence of any substrate or in the presence of either ATP/EDTA or maltose binding protein show their maxima between 2.0 nm and 2.2 nm and thus appear more closed [16,42]. For the vanadate-trapped conformer, which mimics the transition state during ATP hydrolysis, an average distance of 1.6 nm was reported, close to that of the post hydrolysis state [42]. The distributions of the distance between the homologous positions 101 and 101′ in $HisP_2$ closely resemble those observed experimentally for 83 and 83′ in $MalK_2$ in all states investigated (Fig. 3c). This agreement in the distance distributions of these two systems is strong evidence that the NBDs in the $HisQMP_2$ complex in the presence of HisJ and substrate undergo similar conformational transitions as $MalK_2$ in $MalFGK_2$, although the C-terminal extension present in MalK is missing in HisP. In addition, the relative arrangements of at least the Q-loops in the HisP dimer must be very similar to those of the MalK dimer in all states examined.

The presence of HisJ is crucial for complete closure of the NBDs to occur. In the absence of HisJ, ATP binding induced only minor if any distance changes between the two HisP subunits (Fig. 2b). This correlates to the strongly suppressed ATP-hydrolysis rates. In contrast, the addition of liganded HisJ and ATP induced a tighter closure of the NBDs. HisJ binding is thus correlated to structural rearrangements which are transferred through the TMDs to the cytoplasmic coupling helices to induce the closure of the NBDs. This result provides the structural link to ATP hydrolysis stimulation. The results of a most recent study using limited proteolysis as an alternative tool to monitor conformational changes of the histidine transporter are consistent with this notion. Here, it was demonstrated that distinct cleavage sites in HisP and HisQ are rendered insusceptible to protease in the presence of liganded binding protein and ATP only, thus also indicating transmembrane signaling by the substrate [52]. The hydrolysis induced conformational transitions of the NBDs is transferred to the transmembrane helices as monitored by the distance changes between positions 118 and 123. In the apo-state the arrangement of the cytoplasmic ends of helices 3 and 3′ differs from those in the closed and semi-open states. The distance distributions of the latter are shifted to smaller distance values compared to the apo state. Hence, the changes in distances across this part of the cytoplasmic gate very much resemble those observed for the Q-loop positions 101/101′. The normal mode analysis provides evidence for a concerted motion of this part of the cytoplasmic gate, the Q-loop positions 101/101′ and the NBDs′ center of mass.

For the maltose transporter we know that the opening or closing of the maltose binding protein, MBP, coincides with transitions between the semi-open and the closed conformation of the MalK dimer rather than between the open and the semi-open configurations [6]. Indeed,

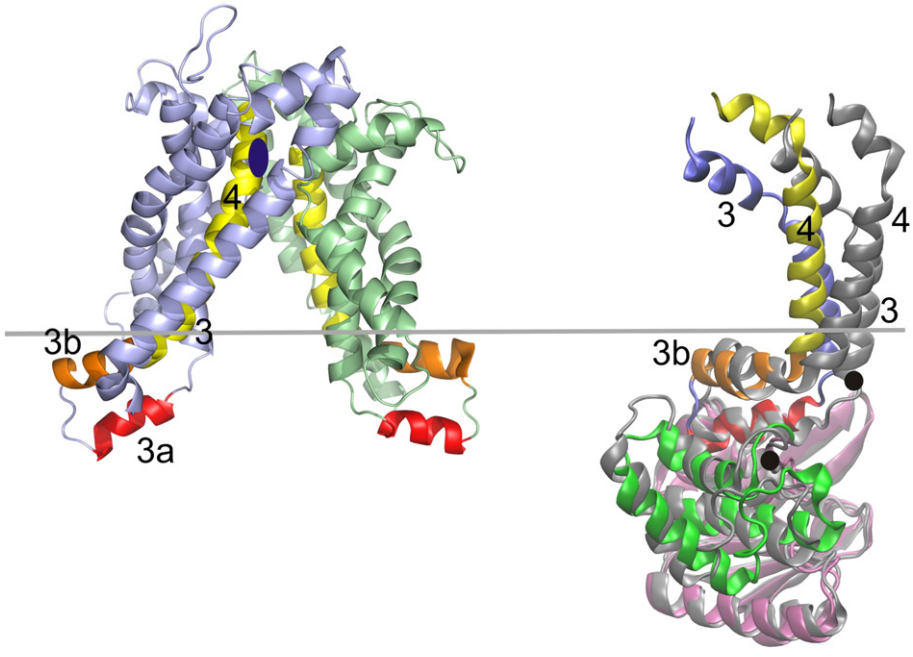


**Fig. 4.** Conformation and conformational changes of the transmembrane subunits as revealed by the HisQM model and crystal structures of $MalFGK_2$. *Left*: Transmembrane subunits HisQ (blue) and HisM (green) with coupling helices 3a (red), helices 3b (orange) and the membrane-spanning helices 4 (yellow). The location of HisQ–K163 in helix 4 is highlighted by a blue ellipse, the location of the membrane–cytoplasm interface is indicated by a gray line. *Right*: Close-up of the cytoplasmic moiety of MalF in contact with MalK reveals the conformational differences in helix 4 positions. Open (gray) and closed (colored according to the HisQM model, *left*) conformations are superimposed based on best fitting of the RecA-like subdomain to visualize the helical movement in the α-helical subdomain of MalK and the reorientations of helices 3, 3a, 3b and 4 in MalF. The positions of the spin labeled sites in $HisQMP_2$ (118 at the C-terminus of helix 3, and 101 in the Q-loop of the NBD) according to the model (Fig. 1a) are indicated by black dots.

the closed (ATP-bound) and semi-open (post hydrolysis) states of $HisP_2$ lead to clearly distinguishable distance distributions with average distance changes of more than 1 nm for the pair 197R1–104R1 at the periplasmic side of HisQM. Hence, the conformational transition of the NBDs from the closed to the semi-open conformation is transferred to the periplasmic side of the TMDs. Since the difference in distance distributions between positions 118 and 123 for these two states are small as they are indistinguishable in our measurements it is unlikely that this communication occurs via helix 3. EPR experiments have shown that the closed and semi-open states of $MalK_2$ are coupled to a reorientation of the α-helical subdomain from an inward to an outward orientation [51]. This leads to a shift of the coupling helix 3a and of helix 3b, which are closely connected by a short loop and inter-helical hydrophobic interaction. On the other hand, helix 3b is rigidly connected to transmembrane helix 4 by conserved P144 in HisQ or P153 in HisM. A reorientation of helix 3b thus may communicate the conformational transitions to the periplasmic side via a reorientation of helix 4 similar to that found in $MalFGK_2$ as depicted in Fig. 4. The important role of a possible movement of helix 4 in the gating mechanism in HisQM is corroborated by the observation that the exchange of residues K163 in HisQ or H172 in HisM, which according to the model are located in the periplasmic gate region (see Fig. 4), leads to a loss of function [33].

The distances measured between spin labels at the periplasmic side of the TMDs reveal at least two different conformations to be distinguishable. The largest change in distances for the pair 197R1–104R1 occurs upon the transition from the ATP-bound to the post hydrolysis state. This may indicate the conformational transition of the periplasmic moiety of the TMDs, which accompanies the periplasmic gating and the putative communication with HisJ. Similarly, the results provide evidence that the distance for the apo and the nucleotide bound states differ for the pair 86R1–96R1. Although the analysis of this mutant is hampered by the broad distance distribution, the experiments reveal that the conformational changes in different parts of the periplasmic gate are complex and may be modulated by the interaction with the substrate binding protein HisJ. Further studies characterizing the interaction with HisJ during substrate transport will be necessary to understand the details of these conformational changes.

We have shown that the arrangement of the Q-loop positions 101/101′ in the HisP dimer in the membrane reconstituted $HisQMP_2$ complex and its conformational changes during the nucleotide hydrolysis cycle resemble that of the homologous positions 83/83′ in the MalK dimer. This is strong evidence that the model based on the maltose system is applicable to $HisQMP_2$ as far as the conformational alterations of the NBDs and communication with the TMDs are concerned. Based on our experimental observations the communication of the closed and semi-open states to the periplasmic side along helix 3 seems to be unlikely, since the difference in the distance between positions 118 and 123 for the ATP bound and post hydrolysis states is minor. We rather suggest a rearrangement of helix 4 during the closed to the semi-open transition of $HisP_2$ driven by the reorientation of the coupled helices 3a and 3b to occur upon hydrolysis, again in agreement with the results on $MalFGK_2$ [51]. In spite of the lack of clear oscillations in the DEER traces for some of the spin labeled TMD samples, conformational states can be distinguished for the periplasmic moiety of HisQM which are correlated to the proposed open, semi-open and closed states of $HisP_2$.

## Acknowledgements

We thank C. Schwan and F. Ronnebaum for EPR measurements. This work was supported by the Deutsche Forschungsgemeinschaft PAK 459 (SCHN 274/14-1 to E.S. and STE 640/10 to H.J.S.) and by a fellowship from the Department of Biology, HU Berlin, to D.W.

## Appendix A. Supplementary data

Supplementary data to this article can be found online at http://dx.doi.org/10.1016/j.bbamem.2014.02.010.

## References

[1] I.B. Holland, S.P.C. Cole, K. Kuchler, C.F. Higgins, ABC Proteins: From Bacteria to Man, Academic Press, Inc., New York, 2003.
[2] A. Licht, E. Schneider, ATP binding cassette systems: structures, mechanisms, and functions, Cent. Eur. J. Biol. 6 (2011) 785–801.
[3] A.L. Davidson, E. Dassa, C. Orelle, J. Chen, Structure, function, and evolution of bacterial ATP-binding cassette systems, Microbiol. Mol. Biol. Rev. 72 (2008) 317–364.
[4] T. Eitinger, D.A. Rodionov, M. Grote, E. Schneider, Canonical and ECF-type ATP-binding cassette importers in prokaryotes: diversity in modular organization and cellular functions, FEMS Microbiol. Rev. 35 (2011) 3–67.
[5] R.P.A. Berntsson, S.H.J. Smits, L. Schmitt, D.J. Slotboom, B. Poolman, A structural classification of substrate-binding proteins, FEBS Lett. 584 (2010) 2606–2617.
[6] C. Orelle, T. Ayvaz, R.M. Everly, C.S. Klug, A.L. Davidson, Both maltose-binding protein and ATP are required for nucleotide-binding domain closure in the intact maltose ABC transporter, Proc. Natl. Acad. Sci. U. S. A. 105 (2008) 12837–12842.
[7] B.H. Shilton, The dynamics of the MBP-MalFGK2 interaction: a prototype for binding protein dependent ABC-transporter systems, Biochim. Biophys. Acta Biomembr. 1778 (2008) 1772–1780.
[8] K.P. Locher, Structure and mechanism of ATP-binding cassette transporters, Philos. Trans. R. Soc. B Biol. Sci. 364 (2009) 239–245.
[9] V.M. Korkhov, S.A. Mireku, K.P. Locher, Structure of AMP–PNP-bound vitamin B12 transporter BtuCD-F, Nature 490 (2012) 367–372.
[10] O. Lewinson, A.T. Lee, K.P. Locher, D.C. Rees, A distinct mechanism for the ABC transporter BtuCD–BtuF revealed by the dynamics of complex formation, Nat. Struct. Mol. Biol. 17 (2010) 332–338.
[11] B. Joseph, G. Jeschke, B.A. Goetz, K.P. Locher, E. Bordignon, Transmembrane gate movements in the type II ABC importer BtuCD-F during nucleotide cycle, J. Biol. Chem. 286 (2011) 41008–41017.
[12] E. Vigonsky, E. Ovcharenko, O. Lewinson, Two molybdate/tungstate ABC transporters that interact very differently with their substrate binding proteins, Proc. Natl. Acad. Sci. 110 (2013) 5440–5445.
[13] E. Bordignon, M. Grote, E. Schneider, MicroReview: the maltose ATP-binding cassette transporter in the 21st century — towards a structural dynamic perspective on its mode of action, Mol. Microbiol. 77 (2010) 1354–1366.
[14] J. Chen, Molecular mechanism of the *Escherichia coli* maltose transporter, Curr. Opin. Struct. Biol. 23 (2013) 492–498.
[15] D.C. Rees, E. Johnson, O. Lewinson, ABC transporters: the power to change, Nat. Rev. Mol. Cell Biol. 10 (2009) 218–227.
[16] M. Grote, Y. Polyhach, G. Jeschke, H.-J. Steinhoff, E. Schneider, E. Bordignon, Transmembrane signaling in the maltose ABC transporter MalFGK2-E: periplasmic MalF-P2 loop communicates substrate availability to the ATP-bound MalK dimer, J. Biol. Chem. 284 (2009) 17521–17526.
[17] S. Böhm, A. Licht, S. Wuttge, E. Schneider, E. Bordignon, Conformational plasticity of the type I maltose ABC importer, Proc. Natl. Acad. Sci. 110 (2013) 5492–5497.
[18] E. Schneider, S. Hunke, ATP-binding-cassette (ABC) transport systems: functional and structural aspects of the ATP-hydrolyzing subunits/domains, FEMS Microbiol. Rev. 22 (1998) 1–20.
[19] M.L. Oldham, D. Khare, F.A. Quiocho, A.L. Davidson, J. Chen, Crystal structure of a catalytic intermediate of the maltose transporter, Nature 450 (2007) 515–521.
[20] M.L. Daus, S. Berendt, S. Wuttge, E. Schneider, Maltose binding protein (MalE) interacts with periplasmic loops P2 and P1 respectively of the MalFG subunits of the maltose ATP binding cassette transporter ($MalFGK_2$) from *Escherichia coli/Salmonella* during the transport cycle, Mol. Microbiol. 66 (2007) 1107–1122.
[21] M.L. Daus, M. Grote, E. Schneider, The MalF P2 loop of the ATP-binding cassette transporter MalFGK2 from *Escherichia coli* and *Salmonella enterica* serovar Typhimurium interacts with maltose binding protein (MalE) throughout the catalytic cycle, J. Bacteriol. 191 (2009) 754–761.
[22] T. Jacso, M. Grote, M.L. Daus, P. Schmieder, S. Keller, E. Schneider, B. Reif, Periplasmic loop P2 of the MalF subunit of the maltose ATP binding cassette transporter is sufficient to bind the maltose binding protein MalE, Biochemistry 48 (2009) 2216–2225.
[23] T. Jacso, E. Schneider, B. Rupp, B. Reif, Substrate transport activation is mediated through second periplasmic loop of transmembrane protein MalF in maltose transport complex of *Escherichia coli*, J. Biol. Chem. 287 (2012) 17040–17049.
[24] J. Chen, G. Lu, J. Lin, A.L. Davidson, F.A. Quiocho, A tweezers-like motion of the ATP-binding cassette dimer in an ABC transport cycle, Mol. Cell 12 (2003) 651–661.
[25] E. Schneider, ABC transporters catalyzing carbohydrate uptake, Res. Microbiol. 152 (2001) 303–310.
[26] G.F.-L. Ames, K. Nikaido, I.X. Wang, P.Q. Liu, C.E. Liu, C. Hu, Purification and characterization of the membrane-bound complex of an ABC transporter, the histidine permease, J. Bioenerg. Biomembr. 33 (2001) 79–92.
[27] E. Schneider, Import of solutes by ABC-transporters — the maltose and other systems, in: I.B. Holland, S. Cole, K. Kuchler, C.F. Higgins (Eds.), ABC Proteins: From Bacteria to Man, Academic Press, Inc., New York, 2003.
[28] L.W. Hung, I.X. Wang, K. Nikaido, P.Q. Liu, G.F.-L. Ames, S.H. Kim, Crystal structure of the ATP-binding subunit of an ABC transporter, Nature 396 (1998) 703–707.

[29] B.-H. Oh, G.F.-L. Ames, S.-H. Kim, Structural basis for multiple ligand specificity of the periplasmic lysine-, arginine-, ornithine-binding protein, J. Biol. Chem. 269 (1994) 26323–26330.
[30] B.-H. Oh, C.-H. Kang, H. De Bondt, S.-H. Kim, K. Nikaido, A.K. Joshi, G.F.-L. Ames, The bacterial periplasmic histidine-binding protein. structure/function analysis of the ligand-binding site and comparison with related proteins, J. Biol. Chem. 269 (1994) 4135–4143.
[31] C.E. Liu, P.Q. Liu, G.F.-L. Ames, Characterization of the adenosine triphosphatase activity of the periplasmic histidine permease, a traffic ATPase (ABC transporter), J. Biol. Chem. 272 (1997) 21883–21891.
[32] K. Nikaido, P.Q. Liu, G.F.-L. Ames, Purification and characterization of HisP, the ATP-binding subunit of a traffic ATPase (ABC transporter), the histidine permease of *Salmonella typhimurium*, J. Biol. Chem. 272 (1997) 27745–27752.
[33] D. Weidlich, N. Wiesemann, J. Heuveling, K. Wardelmann, H. Landmesser, K.B. Sani, C.L. Worth, R. Preissner, E. Schneider, Residues of a proposed gate region in type I ATP-binding cassette import systems are crucial for function as revealed by mutational analysis, Biochim. Biophys. Acta Biomembr. 1828 (2013) 2164–2172.
[34] H.-J. Steinhoff, N. Radzwill, W. Thevis, V. Lenz, D. Brandenburg, A. Antson, G.G. Dodson, A. Wollmer, Determination of interspin distances between spin labels attached to insulin: comparison of electron paramagnetic resonance data with the X-ray structure, Biophys. J. 73 (1997) 3287–3298.
[35] M. Pannier, S. Veit, A. Godt, G. Jeschke, H.W. Spiess, Dead-time free measurement of dipole–dipole interactions between electron spins, J. Magn. Reson. 142 (2000) 331–340.
[36] G. Jeschke, V. Chechik, P. Ionita, A. Godt, H. Zimmermann, J.E. Banham, C.R. Timmel, D. Hilger, H. Jung, DeerAnalysis2006 — a comprehensive software package for analyzing pulsed ELDOR data, Appl. Magn. Reson. 30 (2006) 473–498.
[37] Y. Polyhach, E. Bordignon, G. Jeschke, Rotamer libraries of spin labelled cysteines for protein studies, Phys. Chem. Chem. Phys. 13 (2011) 2356–2366.
[38] E. Eyal, L.W. Yang, I. Bahar, Anisotropic network model: systematic evaluation and a new web interface, Comput. Appl. Biosci. 22 (2006) 2619–2627.
[39] W. Humphrey, A. Dalke, K. Schulten, VMD: visual molecular dynamics, J. Mol. Graph. 14 (1996) 33–38.
[40] D. Frishman, P. Argos, Knowledge-based protein secondary structure assignment, Proteins Struct. Funct. Bioinformatics 23 (1995) 566–579.
[41] A. Bakan, L.M. Meireles, I. Bahar, ProDy: protein dynamics inferred from theory and experiments, Comput. Appl. Biosci. 27 (2011) 1575–1577.
[42] M. Grote, E. Bordignon, Y. Polyhach, G. Jeschke, H.-J. Steinhoff, E. Schneider, A comparative EPR study of the nucleotide-binding domains' catalytic cycle in the assembled maltose ABC-importer, Biophys. J. 95 (2008) 2924–2938.
[43] Y. Polyhach, G. Jeschke, E. Bordignon, MMM (Multiscale Molecular Modelling) 2011, 2011. -121.
[44] J.P. Klare, H.-J. Steinhoff, Site-Directed Spin Labeling and Pulse Dipolar Electron Paramagnetic Resonance, 2010.
[45] M.L. Oldham, J. Chen, Snapshots of the maltose transporter during ATP hydrolysis, Proc. Natl. Acad. Sci. 108 (2011) 15152–15156.
[46] M.L. Oldham, J. Chen, Crystal structure of the maltose transporter in a pretranslocation intermediate state, Science 332 (2011) 1202–1205.
[47] I. Bahar, T.R. Lezon, A. Bakan, I.H. Shrivastava, Normal mode analysis of biomolecular structures: functional mechanisms of membrane proteins, Chem. Rev. 110 (2010) 1463–1497.
[48] A.R. Atilgan, S.R. Durell, R.L. Jernigan, M.C. Demirel, O. Keskin, I. Bahar, Anisotropy of fluctuation dynamics of proteins with an elastic network model, Biophys. J. 80 (2001) 505–515.
[49] G. Lu, J.M. Westbrooks, A.L. Davidson, J. Chen, ATP hydrolysis is required to reset the ATP-binding cassette dimer into the resting-state conformation, Proc. Natl. Acad. Sci. U. S. A. 102 (2005) 17969–17974.
[50] D. Khare, M.L. Oldham, C. Orelle, A.L. Davidson, J. Chen, Alternating access in maltose transporter mediated by rigid-body rotations, Mol. Cell 33 (2009) 528–536.
[51] C. Orelle, F.J. Alvarez, M.L. Oldham, A. Orelle, T.E. Wiley, J. Chen, A.L. Davidson, Dynamics of α-helical subdomain rotation in the intact maltose ATP-binding cassette transporter, Proc. Natl. Acad. Sci. 107 (2010) 20293–20298.
[52] J. Heuveling, V. Frochaux, J. Ziomkowska, R. Wawrzinek, P. Wessig, A. Herrmann, E. Schneider, Conformational changes of the bacterial type I ATP-binding cassette importer HisQMP2 at distinct steps of the catalytic cycle, Biochim. Biophys. Acta Biomembr. 1838 (2014) 106–116.
[53] V. Eckey, D. Weidlich, H. Landmesser, U. Bergmann, E. Schneider, The second extracellular loop of pore-forming subunits of ATP-binding cassette transporters for basic amino acids plays a crucial role in interaction with the cognate solute binding protein(s), J. Bacteriol. 192 (2010) 2150–2159.